Spurious Arrivals in Teleseismic Noise Correlations Explained by a Quasi-Stationary Phase Condition

Lei Li, Pierre Boué, and Michel Campillo

Université Grenoble Alpes, CNRS, IRD, IFSTTAR, ISTerre, 38000 Grenoble, France.

Corresponding author: Lei Li (ll.ynyf@gmail.com)

Abstract

Traditionally, the reconstruction of seismic phases from inter-receiver noise correlations is attributed to the interference between waves from noise sources in the stationary-phase regions. With seismic noise records from two networks at teleseismic distance, we show that spurious signals having no correspondence in real seismograms can arise from interference between waves without common ray path or common slowness. These noise-derived signals cannot be explained by traditional stationary-phase arguments. These signals still emerge for evenly distributed noise sources, and thus are not caused by localized sources. With numerical experiments, we interpret the presence of the spurious signals with a condition of quasi-stationary phase: when time delays between interfering waves from spatially distributed noise sources are close enough, the stack of correlation functions over the distributed sources can be constructive, and thereby noise-derived signals emerge from the source averaging.

1 Introduction

The technique of noise correlation is implemented simply via computation of the correlation functions between ambient noise records at receivers. Theoretical and experimental studies (e.g., Lobkis & Weaver, 2001; Wapenaar, 2004) have shown that under restrictive conditions, the inter-receiver correlation function converges toward the response that would be recorded at one receiver if a source was located at the other. This is, by definition, the Green's function of the medium between the two receivers. Great achievements have been realized with the introduction of the noise correlation technique into solid-Earth seismology (Campillo & Paul, 2003; Shapiro & Campillo, 2004). The most common applications are passive imaging (e.g., Sabra et al., 2005; Shapiro et al., 2005) and monitoring (e.g., Brenguier et al., 2008; Wegler et al., 2009) of the subsurface using signals derived from seismic noise. We refer to (Campillo & Roux, 2015) for a systematic review on the recent progress in the theoretical and methodological aspects, and the various noise-based applications.

Both the surface-wave and body-wave parts of the Green's function can be reconstructed from noise correlations. Surface waves are easier to extract due to their dominance in the noise power spectra. There are relatively few, yet promising, examples of noise-derived body waves.

Recently, it has been demonstrated that deep body-wave signals that propagate through the mantle and core can be extracted from ambient noise correlations (e.g., Boué et al., 2013, 2014; Nishida, 2013). In contrast to previous studies that have primarily discussed the reconstruction of normal seismic phases from noise correlations, we focus our analysis here on interpretation of a spurious phase that can be observed from noise correlations between receivers separated at teleseismic distances. A seismic phase is termed normal if it is present in the Green's function of the medium, and spurious if it is not observed in real seismograms and does not obey the theory of seismic wave propagation. First, we correlate seismic noise records from the Full Range Seismograph Network of Japan (the FNET array) and the northern Fennoscandia POLENET/LAPNET seismic network (the LAPNET array). Then, we develop a new technique to analyze the origin of the spurious phase, and propose a mechanism to explain its presence.

2 Processing of Noise Data

Continuous seismograms recorded by the broadband stations of the FNET and LAPNET arrays in 2008 are used to compute the double-array noise correlations (**Figure 1**). The aperture of LAPNET is ~700 km, and that of FNET is nearly 1,400 km. There are 1,558 FNET–LAPNET station pairs in all. The distance between the FNET and LAPNET stations ranges from ~56° to 70°, with a center-to-center distance of 63°.

Segment-based processing of noise data is demonstrated in **Figure S1**. First, we apply routine signal-processing operations to the raw seismograms (i.e., mean and linear trend removal, filtering, 5 Hz down-sampling, instrumental response deconvolution). Then, we divide the continuous seismograms into 4-hour segments. The frequency spectra of the segments are whitened between periods of 1 s and 100 s. This spectral whitening removes amplitude information and retains only the phase spectrum. The whitened waveform is clipped at 3.8 times the standard deviation. A selection filter is applied to the segments to detect and reject those containing transient impulses, like earthquakes and electronic glitches.

The processing is similar to that adopted by Poli et al. (2012) and Boué et al. (2013). The main difference is that we use a new kurtosis-based selection filter to detect and reject segments dominated by impulsive transients. The kurtosis is defined as $\kappa = \mathbf{E}[s^4]/(\mathbf{E}[s^2])^{\mathbf{2}} - 3$, with $\mathbf{E}[\cdot]$ the expectation operator and s the demeaned waveform. It is highly sensitive to impulsiveness (Westfall, 2014), close to zero for stationary noise and increases abruptly in the presence of transient impulses (see **Figure S2** for practical examples). Segments of kurtosis beyond 1.5 are discarded. In the previous studies, the detection was based on the energy ratio between segment and daily trace, a coarse version of the classic STA/LTA method for earthquake detection (Allen, 1982). Compared to the energy-based detection, the kurtosis-based detection depends on the statistics of the amplitudes of the segment itself and is more reliable when the strength of seismic noise changes rapidly. The kurtosis-based detection has also been used in earthquake detection (e.g., Baillard et al., 2014; Saragiotis et al., 2002).

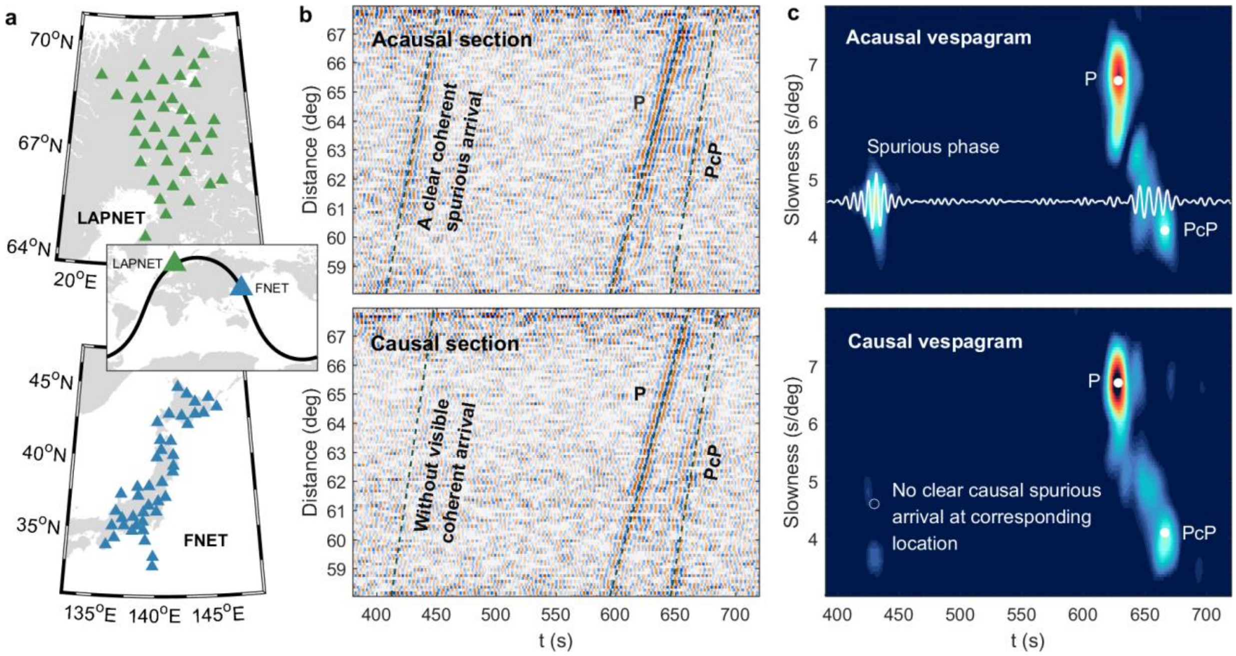

Figure 1. (a) Geographic distributions of the 38 stations of the LAPNET array in Finland, and 41 stations of the FNET array in Japan. Dark line (global map inset), the great circle across the two networks. **(b)** Waveform sections and **(c)** vespagrams of the acausal and causal parts of the vertical–vertical noise correlations filtered in the secondary microseism period band from 5 s to 10 s. Dashed lines (b), predicted time–distance curves. Solid white dots (c), theoretical P and PcP arrivals, as predicted by the *Taup* program (Crotwell et al., 1999) and the *IASP91* Earth model (Kennett & Engdahl, 1991). It can be estimated from the acausal vespagram that at 63° distance between the FNET and LAPNET array centers, the spurious phase has an arrival time of 430 s and an apparent slowness of 4.6 s/deg. The waveform beamed by 4.6 s/deg slowness is plotted overlying the acausal vespagram.

3 Observation of Noise-Derived Spurious Phase

The calculation of correlation function is explained in **Figure S3**. To produce the correlation function of the year-long data for each FNET–LAPNET station pair, we correlate all of the available pairs of processed noise segments and stack them. The correlation function has a causal part and an acausal part. In this paper, the acausal correlations correspond to seismic waves that travel from FNET to LAPNET (causal: from LAPNET to FNET).

The noise correlations of all of the FNET–LAPNET station pairs are binned in an inter-station distance interval of 0.1°, to produce the waveform sections for the acausal and causal parts of the noise correlations. The broadband sections of vertical–vertical noise correlations are shown in **Figure S4** and the filtered sections (periods of 5 s to 10 s) in **Figure 1b**. A coherent arrival between 410 s and 450 s is clearly visible in the acausal section, about 200 s earlier than the direct P wave that should be the primary arrival. The arrival has no correspondence in the true Green's function of the Earth medium, and thereby is undoubtedly a spurious phase. From the acausal vespagram in **Figure 1c**, the apparent slowness and emerging time of the spurious phase at 63° distance can be estimated: ~4.6 s/deg and 430 s, respectively. Spectral analysis indicates that the spurious phase has a peak period of 6.2 s (**Figure S5**), a typical value for the secondary microseism that is the largest peak in the seismic noise spectra (Peterson, 1993). Secondary microseisms are dominantly excited by ocean wave–wave interactions (Hasselmann, 1963; Longuet-Higgins, 1950), implying that the noise sources are mainly distributed on the global ocean surface. In the causal correlations, a corresponding spurious phase is hardly discriminable.

4 Origin of Spurious Phase from P–PKPab Correlations

In the previous section, a prominent spurious phase was observed in the FNET–LAPNET noise correlations, and its apparent slowness and emerging time were estimated. The double-array configuration provides the possibility to estimate both the azimuths and magnitudes of the slownesses of the correlated wavefields responsible for the spurious phase. Given a wave with slowness $\boldsymbol{p}^A$ at FNET and a wave with slowness $\boldsymbol{p}^B$ at LAPNET, the time delay between the *i*th FNET station and the *j*th LAPNET station can be determined from Equation (1):

$$\Delta t_{ij} = \boldsymbol{x}_i^A \cdot \boldsymbol{p}^A + \boldsymbol{x}_j^B \cdot \boldsymbol{p}^B \quad (1),$$

where $\boldsymbol{x}$ are the local coordinates of the station with respect to the array center, and superscripts *A* and *B* distinguish between FNET and LAPNET, respectively. For a given pair of $(\boldsymbol{p}^A, \boldsymbol{p}^B)$, the noise correlations of all station pairs are beamed by Equation (2):

$$B(t, \boldsymbol{p}^A, \boldsymbol{p}^B) = \langle\, C_{ij}\big(t - \Delta t_{ij}\big)\rangle \quad (2),$$

where C_{ij} is the correlation function between the *i*th FNET station and the *j*th LAPNET station, and $\langle\cdot\rangle$ indicates the ensemble average. This delay-and-sum process for the double-array data is known as the double-beam method, which has been applied to earthquake data (e.g., Krüger et al., 1993; Rost & Thomas, 2002) and noise correlations (e.g., Boué et al., 2013; Roux et al., 2008). Repeating the double-beamforming for a range of $\boldsymbol{p}^A$ and $\boldsymbol{p}^B$, the power map of the double-beamed waveforms indicates the optimal slowness estimates for the correlated waves. Here we call this method the double-array slowness analysis.

The results for the spurious phase are shown in **Figure 2a**. The azimuths of the correlated waves responsible for the spurious phase are confined to the great-circle direction across FNET and LAPNET, implying that the microseism noise source should be located on the great circle. The slowness at FNET (4.7 s/deg) is distinct from that at LAPNET (4.2 s/deg). We also apply the double-array slowness analysis to the acausal P waves (**Figure S6a**). The slownesses of the interfering waves coincide with each other and are close to the predicted value (6.7 s/deg in *IASP91* model), as expected for the P–PP correlation in a radially layered Earth structure (**Figure S6b**). The P-wave results justify the reliability of these slowness estimates, and show that lateral heterogeneity does not cause the slowness discrepancy observed from **Figure 2a**.

The 4.7 s/deg slowness at FNET is valid for deep mantle phases, and the 4.2 s/deg slowness at LAPNET is characteristic of core phases. We propose a slowness-track method to seek the ray paths of the interfering waves that produce the spurious phase (**Figure 2b**). All the body phases that are discernible in the vertical-component earthquake seismograms are considered as candidates (see labels in **Figure S7**). For a specific seismic phase, the distance from source to receiver can be derived from the slowness. The pairs of seismic phases are rejected if the difference between the distances from the source to the receivers differs from 63° or if their time delay deviates from 430 s. For clarity, only several typical P-type phases (P, PcP, PP, and PKP branches) are shown in **Figure 2b**.

Finally, we find that the correlation between the P wave at ~89° distance and the PKPab wave at ~152° distance is the only combination that satisfies all the constraints. Thus, we can locate the source responsible for the acausal and causal spurious phase, at around [45°S, 174°E] and [12°S, 28°W], respectively. Recall that the spurious phase is not observable in the causal correlations. Comparisons with hindcast ocean wave heights and microseism excitation (**Figure 2c, d**) indicate that the time asymmetry can be explained by the difference in the strength of the noise sources: the acausal source in the ocean south of New Zealand is energetic, whereas the causal source in the low-latitude Atlantic east of Brazil is weak.

The slownesses estimated from the double-array slowness analysis are crucial for the exclusive determination of the interfering waves. Several pairs of seismic phases will meet the apparent slowness and emerging time of the spurious phase. As can be seen from **Figure 2b**, at 89° distance, the PcP wave arrives almost simultaneously with the P wave, which means that PcP–PKPab also has a time delay of ~430 s at 63° inter-receiver distance. **Figure S8** shows another example of PcS–PcPPcP that also satisfies the given time delay and inter-station distance as proposed by Pham et al. (2018) for a spurious phase emerging at similar time delay, but in the context of earthquake coda correlations. However, these waves do not match the slownesses estimated from **Figure 2a**. We interpret this such that compared to the prominent direct P and PKPab waves, the core reflections and their surface multiples are faint phases and have minor contributions to the construction of the spurious phase from the noise correlations.

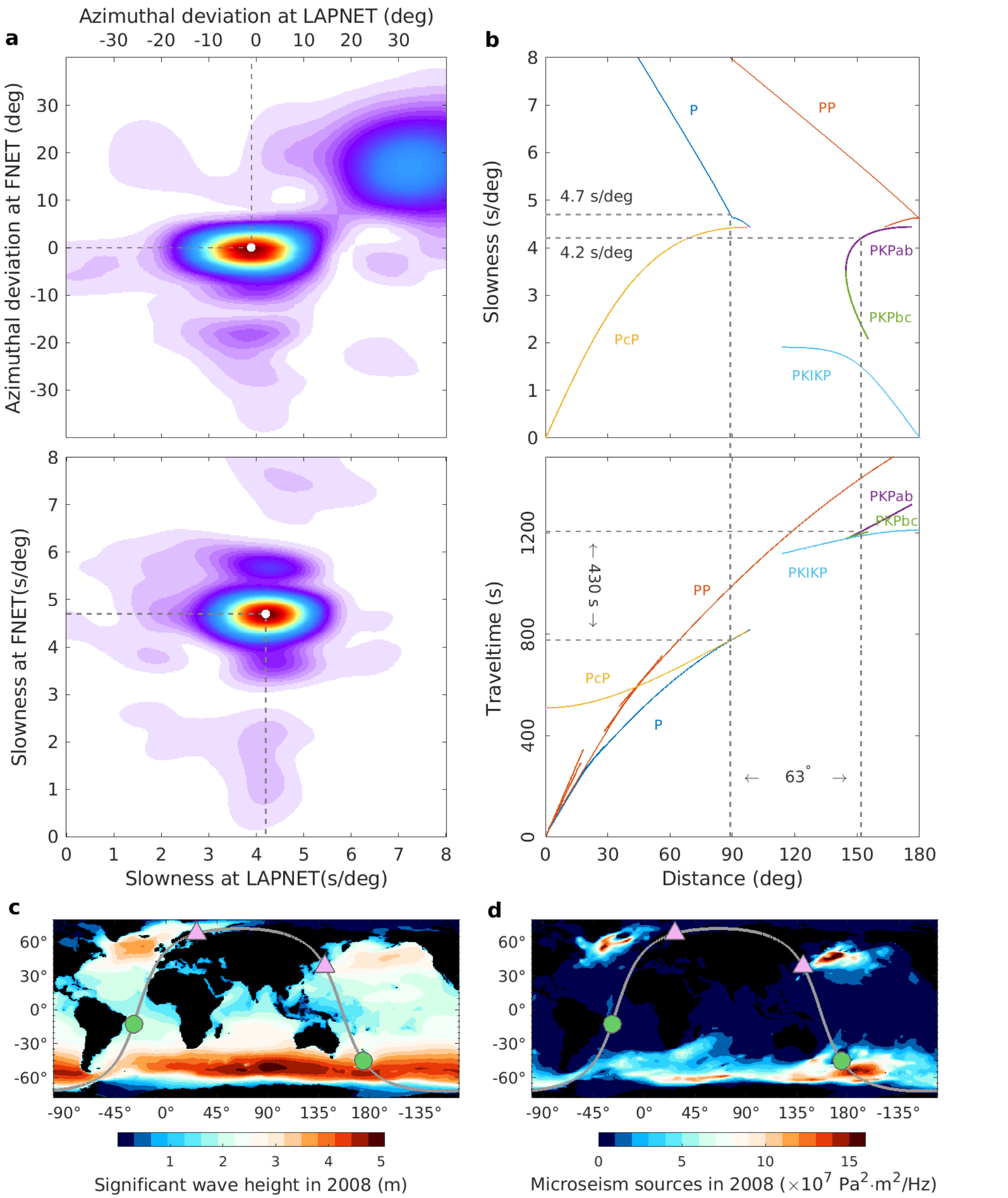

Figure 2. (a) Results of the double-array slowness analysis for the acausal spurious phase. White dots indicate optimal estimates for the azimuths and magnitudes of the slownesses of the interfering waves at FNET and LAPNET that lead to the generation of the spurious phase. The azimuthal deviation refers to the clockwise azimuthal deviation of slowness from the sagittal plane crossing FNET and LAPNET. The azimuthal deviations are almost zero. The slowness values of the interfering waves are 4.7 s/deg at FNET and 4.2 s/deg at LAPNET. **(b)**

Determination of the interfering waves responsible for the spurious phase. The theoretical curves of the ray parameters and the travel-times are calculated using the *Taup* program and the *IASP91* Earth model. The global maps show the spatial distributions of **(c)** the significant wave height, and **(d)** the 6.2 s period secondary microseism excitation in 2008 (Rascle & Ardhuin, 2013). Triangles, locations of FNET and LAPNET; circles, locations of the microseism noise sources responsible for the spurious phase. The source responsible for the acausal spurious phase is located in the ocean south of New Zealand.

5 Quasi-Stationary Phase

The observed spurious phase originates from the correlation between teleseismic P waves and PKPab waves that emanate from the oceanic microseism noise source south of New Zealand. In this section, we explain how such spurious signals arise from the interference between waves of distinct slownesses. Considering the ambient noise wavefield as a superposition of waves from uncorrelated sources distributed on Earth's surface (**Figure 3a**), the correlation function between the noise records at two receivers is equivalent to a stack of the correlation functions for individual sources (source averaging).

We first simulate the source-wise correlation functions by convolving a wavelet of 6.2 s period with the time delays between the two correlated phases. The final inter-receiver correlation is obtained by stacking over all sources. In this ray-based simulation, amplitude information is neglected. The result for the P–PKPab correlations is shown in **Figure 3b**. The construction of signals from noise correlations has been proposed in relation to the stationary-phase condition (e.g., Wapenaar et al., 2010). As an illustration, **Figure S6** shows an example of the reconstruction of the teleseismic P wave that results from the correlation of the P and PP waves. The reconstruction is linked to the extreme (stationary) point on the curve of the P–PP time delay. The P and PP waves from the source at the stationary-phase location (**Figure S6**, source *A*) have a common path and a common slowness. However, as for the spurious phase observed between FNET and LAPNET, the correlated P and PKPab waves have no slowness or ray path in common, and there is no stationary point on the curve of the P–PKPab time delay (**Figure 3b**). The stationary-phase condition is not satisfied, and thus the emergence of the spurious phase cannot be explained by this argument.

Figure 3b shows that for finite-frequency waves, the interference between the P and PKPab waves is constructive over the shaded area; this leads to the pulsive signal in the final inter-receiver correlation function. In contrast to the condition of stationary phase, we propose to call this mechanism the condition of quasi-stationary phase, and refer to this range of sources as the quasi-stationary-phase region or effective source region. At short periods (1 s or shorter), numerical tests for the P–PKPab correlations indicate that source averaging can still lead to signals, with narrower effective source region shrinking toward larger source–receiver distances. Repeating the ray-based modeling in **Figure 3b** for various inter-station distances, a full section can be obtained for the synthetic P–PKPab correlations (see next section for broadband simulation result), from which the theoretical time–distance curve of the spurious phase can be picked. The picked curve is the same for the discoid model shown in **Figure 3a** (sources along a circle) and spherical model (sources on global surface). As shown in **Figure 1b**, the theoretical time–distance curve fits well to the observed spurious signals.

Experiences from earthquake observations indicate that PKPbc waves are generally the dominant PKP branch at distances from ~144° (the PKP-wave caustic) to ~153° (Kulhánek, 2002). Microseism studies have also reported that PKPbc waves can be more prominent (e.g., Gerstoft et al., 2008; Landés et al., 2010). However, our analysis reveals that the spurious phase originates from the interference of P waves with PKPab waves, rather than with PKPbc waves. From the source-averaging experiment for the P–PKPbc correlations (**Figure 3c**), it can be seen that the P–PKPbc time delay varies almost linearly against the source–receiver distance, and that the dynamic range of the time delay is broad. Consequently, the signals in the source-wise correlations are out of phase, which leads to a destructive stack.

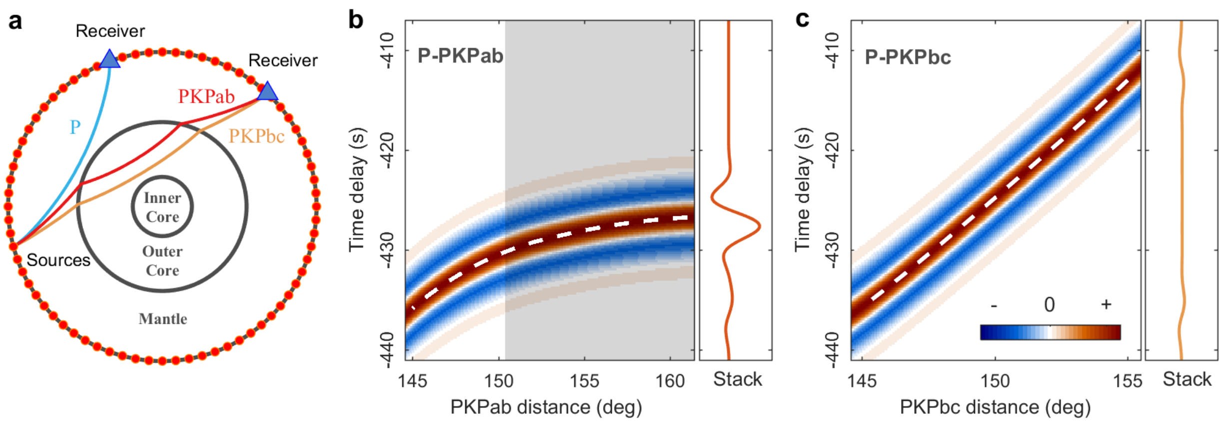

Figure 3. (a) Geometry of the model to synthesize the inter–receiver correlation function of teleseismic P and PKP waves via source averaging. **(b)** P–PKPab correlations for an inter-receiver distance of 63°. Dashed line, time delays between P and PKPab waves emitted from distributed sources. Background image shows the source-wise P–PKPab correlation functions synthesized by convolving the time delays with a 6.2 s period wavelet. The final P–PKPab correlation function by source averaging is plotted in the right panel. The shaded area indicates the range of effective sources that contribute to the signal construction. **(c)** Source-averaging experiment for the P–PKPbc correlations.

6 Effect of Source Distribution

Figure 2d shows that the spatial distribution of the global microseism sources is heavily uneven. The spurious phase is observable in the acausal correlations because the corresponding source is strong, and is not observable in the causal correlations because the responsible source is too weak. In the ray-based synthetic experiments in **Figure 3**, we have neglected the variations of amplitude with wave propagations (geometric spread, inelastic attenuation, reflection and transmission). All of the source-wise correlations are assumed to have the same strength. This simplification ensures that the spurious phase is not likely to be caused by a strong localized source. It is worth determining whether the spurious phase can be eliminated with an ideally uniform source distribution. A formal numerical simulation is made with the waveforms of the P and PKPab waves modeled by the spectral-element method. We obtain the vertical components of the global broadband seismogram for the *iasp91_2s* model (**Figure 4a**), from the IRIS Syngine Data Service (Krischer et al., 2017). A mask is applied to the full waveforms to extract the P waves and the PKPab waves (**Figure 4b**). Assuming that the uncorrelated noise sources are distributed evenly on the global surface, we compute the source-wise correlations and stack them for each inter-station distance, using the data in **Figure 4b**. A global section of correlation functions is obtained accordingly (**Figure 4c**). The spurious phase is clearly reproduced, which suggests that it is not caused by unevenly distributed noise sources.

The ray-based simulation shown in **Figure 4d** mimics well the emerging times of the spurious signals. However, because of the neglect of amplitude information, this approach over-estimates the range of inter-receiver distances where this spurious phase is observable. The simulation based on the waveform here is undoubtedly more realistic.

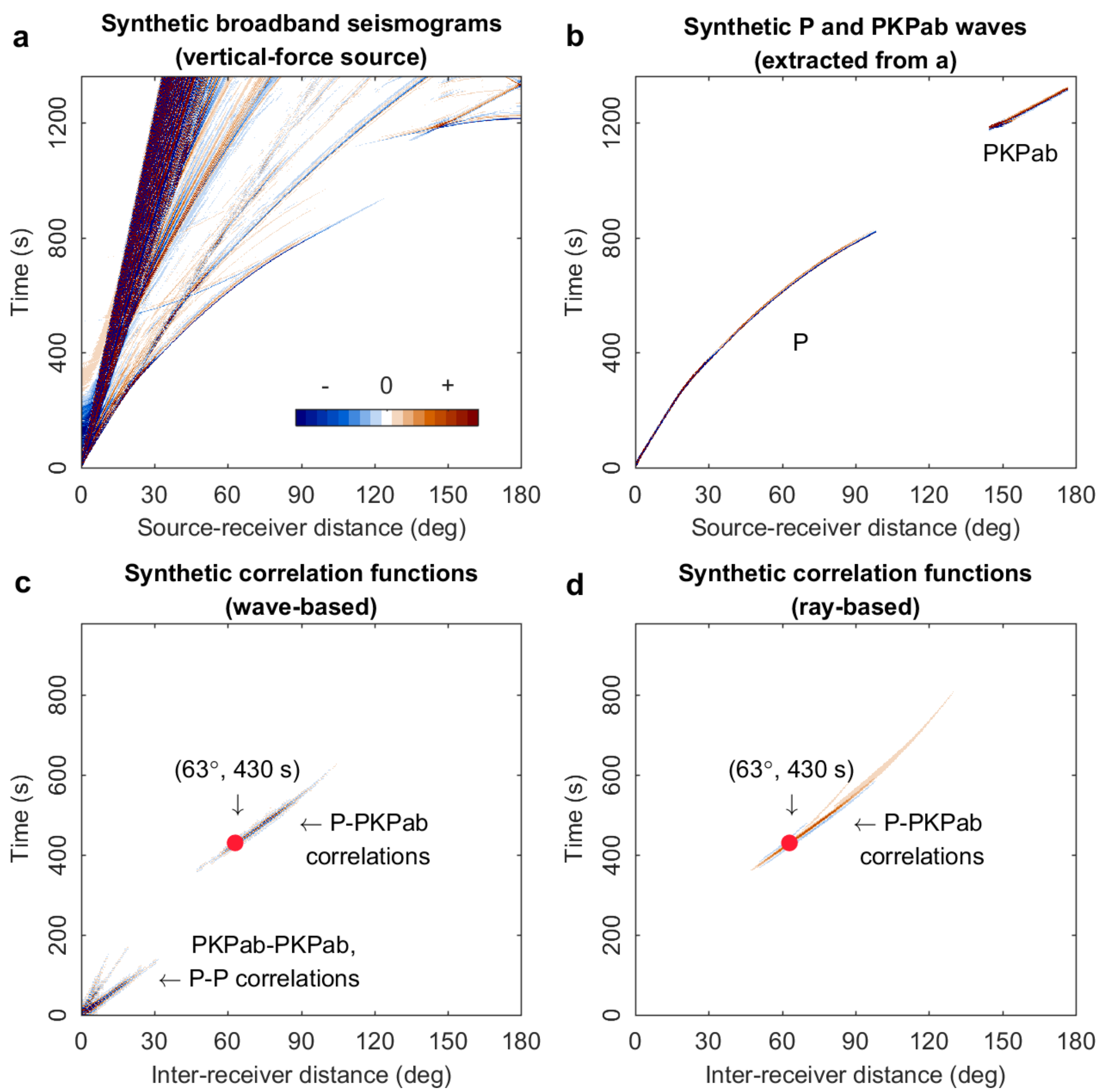

Figure 4. (a) Synthetic broadband (2-100 s) seismograms obtained from the IRIS Syngine Data Service. **(b)** Synthetic seismograms containing P and PKPab only, by muting the other seismic phases in (a). **(c)** Synthetic P–PKPab correlations for the various inter-receiver distances using

the waveform data in (b). **(d)** Synthetic P–PKPab correlations using the ray-based method in **Figure 3**. Red dot, the observed spurious phase.

7 Discussions and Perspectives

We observe an early spurious arrival in the teleseismic noise correlations between the Japan and Finland stations. It arises from interference between the ballistic P waves and PKPab waves that emanate from the oceanic microseism sources south of New Zealand. The interfering waves have deterministic ray paths that sample the Earth deep structure. It is natural to expect that the spurious phase can also be used to investigate the inner structure of the Earth. The spurious phase is observable in the vertical–vertical noise correlations only, which is logical, as the correlated waves are both P-type and their amplitudes are dominantly projected onto the vertical components.

The spurious phase is observable for one side of the correlation functions only. By comparison with oceanic hindcast data, we ascribe this extreme time asymmetry to the large difference in the strength of the microseism sources. The strength of the spurious phase is definitely linked to the microseism excitation in a limited source region. Therefore, another potential application is to monitor the ocean wave activities and microseism excitation.

The P–PKPab correlation is not the unique spurious phase in global noise correlations. Multiple spurious arrivals can be observed from the global sections of the noise correlations constructed with both real and synthetic seismograms (Boué et al., 2013, 2014; Ruigrok et al., 2008). The spurious phase observed in this paper is prominent and isolated from other seismic phases, making it a good example to unveil the generation mechanism of such phases. Based on a double-array slowness analysis, we estimated the respective slownesses of the interfering waves, and tracked the responsible noise source back to New Zealand. This method is also applicable to other spurious phases.

It is important to emphasize the differences between ambient noise and earthquake coda properties. The late coda waves excited by large earthquakes are composed of high-order modes with small slownesses that correspond to core-related reverberations (Maeda et al., 2006; Boué et al., 2014; Poli et al., 2017). The coda wavefields are quite different from the ambient noise wavefields that are dominated by ballistic waves emanating from the distributed noise sources on the Earth's surface. Several spurious phases have been observed in late coda correlations and been interpreted with the traditional stationary-phase arguments (e.g., Pham et al., 2018). Dealing with ambient noise correlations at teleseismic distances, we have shown that the spurious phase observed in this study does not correspond to a stationary point. We propose a less restrictive condition of quasi-stationary phase, which explains our finite-frequency observations.

Acknowledgments and Data

The seismic data of FNET and LAPNET were provided by the National Research Institute for Earth Science and Disaster Resilience (NIED: http://www.fnet.bosai.go.jp) and the Réseau Sismologique & Géodésique Français (RESIF: http://www.resif.fr), respectively. The global sections of the earthquake seismograms and synthetic seismograms were obtained from the IRIS

Data Services (GlobalStacks: https://ds.iris.edu/ds/products/globalstacks/; Syngine: https://ds.iris.edu/ds/products/syngine/). The data of hindcast wave heights and synthetic microseism noise sources were provided by IOWAGA products, as described by (Rascle & Ardhuin, 2013). The computations were performed using the CIMENT infrastructure (https://ciment.ujf-grenoble.fr), which is supported by the Rhône-Alpes region (grant CPER07_13 CIRA: http://www.ci-ra.org). This work is supported by a grant from Labex OSUG@2020 (Investissements d'avenir-ANR10LABX56). The authors also acknowledge the support of the Simone and Cino del Duca Foundation, Insitut de France.

References

Allen, R. (1982). Automatic phase pickers: Their present use and future prospects. *Bulletin of the Seismological Society of America*, *72*(6), S225-242.

Baillard, C., Crawford, W. C., Ballu, V., Hibert, C., & Mangeney, A. (2014). An automatic kurtosis-based P-and S-phase picker designed for local seismic networks. *Bulletin of the Seismological Society of America*, *104*(1), 394–409. https://doi.org/10.1785/0120120347

Boué, P., Roux, P., Campillo, M., & de Cacqueray, B. (2013). Double beamforming processing in a seismic prospecting context. *Geophysics*, *78*(3), V101–V108. https://doi.org/10.1190/geo2012-0364.1

Boué, P., Poli, P., Campillo, M., Pedersen, H., Briand, X., & Roux, P. (2013). Teleseismic correlations of ambient seismic noise for deep global imaging of the Earth. *Geophysical Journal International*, *194*(2), 844–848. https://doi.org/10.1093/gji/ggt160

Boué, P., Poli, P., Campillo, M., & Roux, P. (2014). Reverberations, coda waves and ambient noise: correlations at the global scale and retrieval of the deep phases. *Earth and Planetary Science Letters*, *391*, 137–145. https://doi.org/10.1016/j.epsl.2014.01.047

Brenguier, F., Campillo, M., Hadziioannou, C., Shapiro, N. M., Nadeau, R. M., & Larose, E. (2008). Postseismic relaxation along the San Andreas Fault at Parkfield from continuous seismological observations. *Science*, *321*(5895), 1478–1481. https://doi.org/10.1126/science.1160943

Campillo, M., & Paul, A. (2003). Long-range correlations in the diffuse seismic coda. *Science*, *299*(5606), 547–549. https://doi.org/10.1126/science.1078551

Campillo, M., & Roux, P. (2015). Crust and Lithospheric Structure - Seismic Imaging and Monitoring with Ambient Noise Correlations. In *Treatise on Geophysics* (pp. 391–417). https://doi.org/10.1016/B978-0-444-53802-4.00024-5

Crotwell, H. P., Owens, T. J., & Ritsema, J. (1999). The TauP Toolkit: flexible seismic travel-time and ray-path utilities. *Seismological Research Letters*, *70*(2), 154–160. https://doi.org/10.1785/gssrl.70.2.154

Gerstoft, P., Shearer, P. M., Harmon, N., & Zhang, J. (2008). Global P, PP, and PKP wave microseisms observed from distant storms. *Geophysical Research Letters*, *35*(23), 4–9. https://doi.org/10.1029/2008GL036111

Hasselmann, K. (1963). A statistical analysis of the generation of microseisms. *Reviews of Geophysics*, *1*(2), 177–210. https://doi.org/10.1029/RG001i002p00177

Kennett, B., & Engdahl, E. R. (1991). Traveltimes for global earthquake location and phase identification. *Geophysical Journal International*, *105*(2), 429–465. https://doi.org/10.1111/j.1365-246X.1991.tb06724.x

Krischer, L., Hutko, A. R., van Driel, M., Stähler, S., Bahavar, M., Trabant, C., & Nissen-Meyer, T. (2017). On-demand custom broadband synthetic seismograms. *Seismological Research Letters*, *88*(4), 1127–1140. https://doi.org/10.1785/0220160210

Krüger, F., Weber, M., Scherbaum, F., & Schlittenhardt, J. (1993). Double beam analysis of anomalies in the core-mantle boundary region. *Geophysical Research Letters*, *20*(14), 1475–1478. https://doi.org/10.1029/93GL01311

Kulhánek, O. (2002). The structure and interpretation of seismograms. In *International Geophysics* (Vol. 81, pp. 333–348). Elsevier B.V. https://doi.org/10.1016/S0074-6142(02)80224-8

Landés, M., Hubans, F., Shapiro, N. M., Paul, A., & Campillo, M. (2010). Origin of deep ocean microseisms by using teleseismic body waves. *Journal of Geophysical Research: Solid Earth*, *115*(5), 1–14. https://doi.org/10.1029/2009JB006918

Lobkis, O. I., & Weaver, R. L. (2001). On the emergence of the Green's function in the correlations of a diffuse field. *The Journal of the Acoustical Society of America*, *110*(6), 3011–3017. https://doi.org/10.1121/1.1417528

Longuet-Higgins, M. S. (1950). A theory of the origin of microseisms. *Philosophical Transactions of the Royal Society A: Mathematical, Physical and Engineering Sciences*, *243*(857), 1–35. https://doi.org/10.1098/rsta.1950.0012

Maeda, T., Sato, H., & Ohtake, M. (2006). Constituents of vertical-component coda waves at long periods. *Pure and Applied Geophysics*, *163*(2–3), 549–566. https://doi.org/10.1007/s00024-005-0031-9

Nishida, K. (2013). Global propagation of body waves revealed by cross-correlation analysis of seismic hum. *Geophysical Research Letters*, *40*(9), 1691–1696. https://doi.org/10.1002/grl.50269

Peterson, J. (1993). Observations and modeling of seismic background noise. *U.S. Geol. Surv. Open File Report 93-322*, (No. 93-322).

Phạm, T.-S., Tkalčić, H., Sambridge, M., & Kennett, B. (2018). Earth's correlation wavefield: late coda correlation. *Geophysical Research Letters*, *45*(7), 3035–3042. https://doi.org/10.1002/2018GL077244

Poli, P., Campillo, M., & Pedersen, H. (2012). Body-wave imaging of Earth's mantle discontinuities from ambient seismic noise. *Science*, *338*(6110), 1063–1065. https://doi.org/10.1126/science.1228194

Poli, P., Campillo, M., & de Hoop, M. (2017). Analysis of intermediate period correlations of coda from deep earthquakes. *Earth and Planetary Science Letters*, *477*, 147–155. https://doi.org/10.1016/j.epsl.2017.08.026

Rascle, N., & Ardhuin, F. (2013). A global wave parameter database for geophysical applications. Part 2: model validation with improved source term parameterization. *Ocean Modelling*, *70*, 174–188. https://doi.org/10.1016/j.ocemod.2012.12.001

Rost, S., & Thomas, C. (2002). Array seismology: methods and applications. *Reviews of Geophysics*, *40*(3), 1008. https://doi.org/10.1029/2000RG000100

Roux, P., Cornuelle, B. D., Kuperman, W. a, & Hodgkiss, W. S. (2008). The structure of raylike arrivals in a shallow-water waveguide. *The Journal of the Acoustical Society of America*, *124*(6), 3430–3439. https://doi.org/10.1121/1.2996330

Ruigrok, E., Draganov, D., & Wapenaar, K. (2008). Global-scale seismic interferometry: theory and numerical examples. *Geophysical Prospecting*, *56*(3), 395–417. https://doi.org/10.1111/j.1365-2478.2008.00697.x

Sabra, K. G., Gerstoft, P., Roux, P., Kuperman, W. A., & Fehler, M. C. (2005). Surface wave tomography from microseisms in Southern California. *Geophysical Research Letters*, *32*(14), 1–4. https://doi.org/10.1029/2005GL023155

Saragiotis, C. D., Hadjileontiadis, L. J., & Panas, S. M. (2002). PAI-S/K: A robust automatic seismic P phase arrival identification scheme. *IEEE Transactions on Geoscience and Remote Sensing*, *40*(6), 1395–1404. https://doi.org/10.1109/TGRS.2002.800438

Shapiro, N. M., & Campillo, M. (2004). Emergence of broadband Rayleigh waves from correlations of the ambient seismic noise. *Geophysical Research Letters*, *31*(7), 8–11. https://doi.org/10.1029/2004GL019491

Shapiro, N. M. N., Campillo, M., & Stehly, L. (2005). High-resolution surface-wave tomography from ambient seismic noise. *Science*, *307*(5715), 1615–1618. https://doi.org/10.1126/science.1108339

Wapenaar, K. (2004). Retrieving the elastodynamic Green's function of an arbitrary inhomogeneous medium by cross correlation. *Physical Review Letters*, *93*(25), 254301. https://doi.org/10.1103/PhysRevLett.93.254301

Wapenaar, K., Draganov, D., Snieder, R., Campman, X., & Verdel, A. (2010). Tutorial on seismic interferometry: Part 1 — Basic principles and applications. *Geophysics*, *75*(5), 75A195-75A209. https://doi.org/10.1190/1.3457445

Wegler, U., Nakahara, H., Sens-Schönfelder, C., Korn, M., & Shiomi, K. (2009). Sudden drop of seismic velocity after the 2004 Mw6.6 mid-Niigata earthquake, Japan, observed with Passive Image Interferometry B06305. *Journal of Geophysical Research: Solid Earth*, *114*(6), B06305. https://doi.org/10.1029/2008JB005869

Westfall, P. H. (2014). Kurtosis as peakedness, 1905–2014. R.I.P. *The American Statistician*, *68*(3), 191–195. https://doi.org/10.1080/00031305.2014.917055

Supporting Information

Supplementary Figures S1-S8.

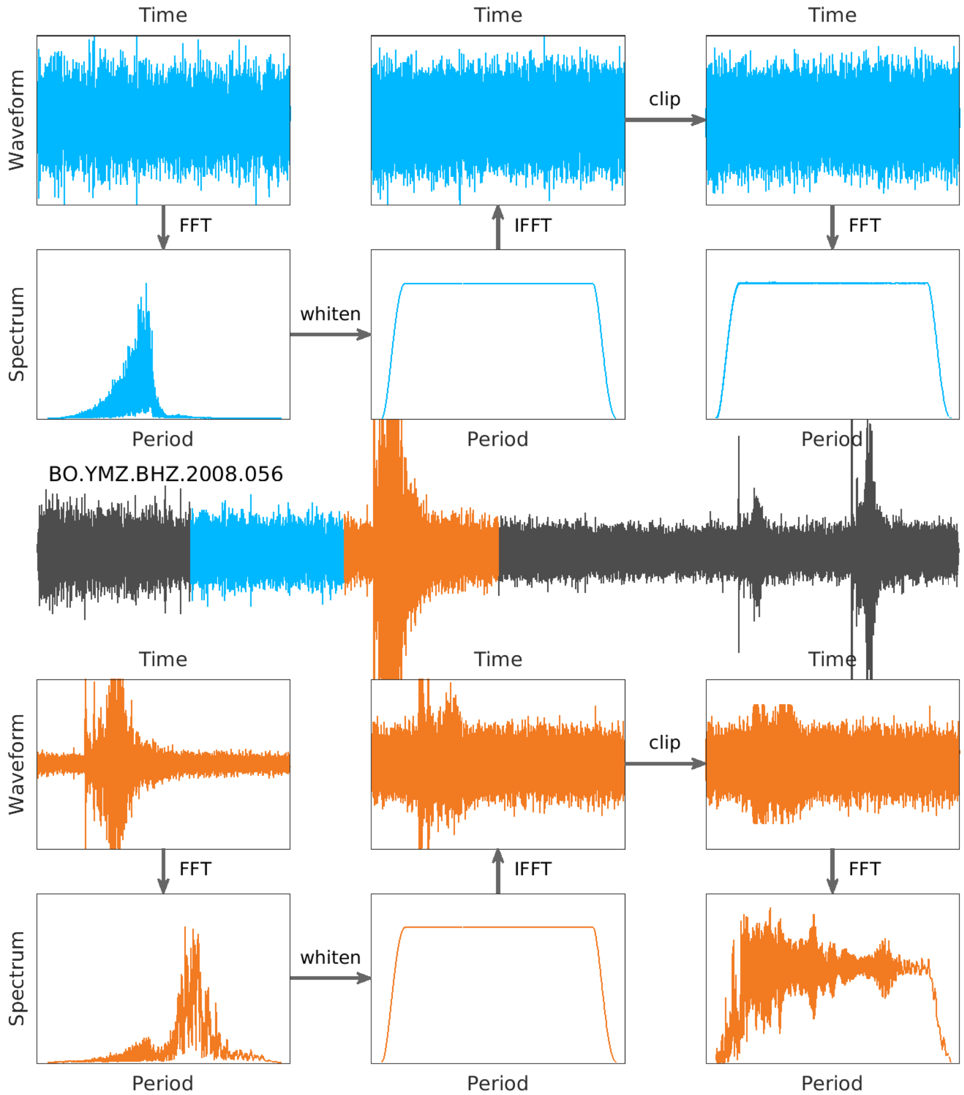

Figure S1. Segment-based noise data processing. A segment with stationary noise and a segment containing a M7.2 teleseism from a daily trace recorded by FNET station BO.YMZ are used for demonstration. The continuous seismogram is demeaned, detrended, bandpass filtered, 5 Hz resampled and instrumental-response removed. Then it is divided into 4-hr segments and their frequency spectra are whitened between 1 and 100 s. One may further clip the spectral-whitened waveform at several times of the standard deviation. The clipping is useful in suppressing large amplitudes in segments with large transients, but has little effect on stationary noise. Thus, the clipping is optional, depending on whether to retain segments with few local spikes. A kurtosis-based selection filter is used to detect and reject segments containing transient impulses like earthquakes and electronic glitches.

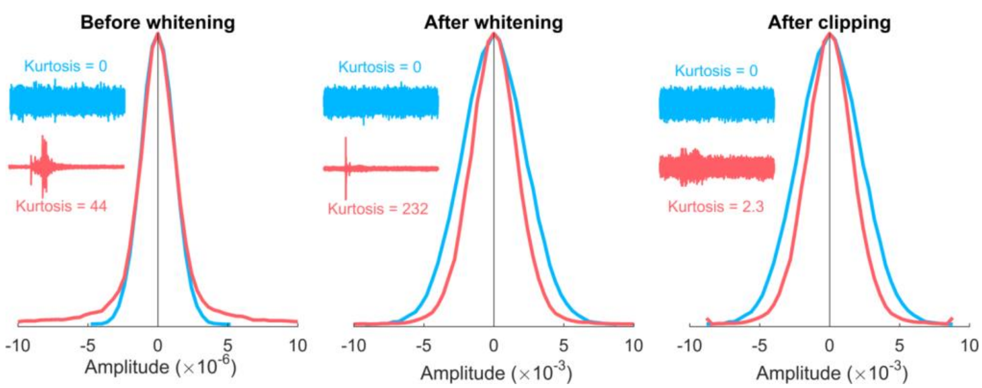

Figure S2. Kurtosis-based selection filter to determine if a segment contains large-amplitude transients. The two segments used here are the same as in Figure S1. The amplitude histograms of the original, spectral-whitened and clipped waveforms are shown in the left, middle and right panels, respectively. For display, waveforms are plotted in different scales. Amplitude histograms are normalized by their own maximums. Histogram tails outside the horizontal axis limits are cropped. The values of kurtosis are labeled. The kurtosis-based selection filter is implemented by rejecting segments with kurtosis beyond a threshold. The selection filter can be applied to any one or more of the three stages shown here. In this paper, we choose a threshold of 1.5 for the clipped segments.

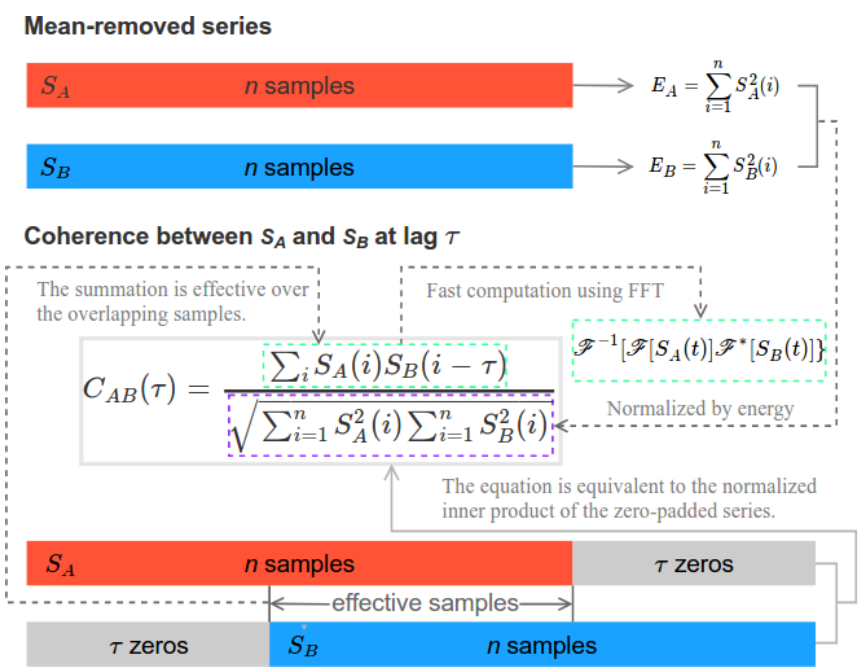

Figure S3. Schematic diagram explaining the computation of correlation function between two mean-removed series. The computation can either be done in the time domain or in the frequency domain. In seismic interferometry, it is common to utilize the Fast Fourier Transform (FFT) for a faster computation of noise correlations. The correlation function contains coherence values for both positive and negative lags between two correlated time series. The part of correlation function at positive (negative) lags is termed causal (acausal).

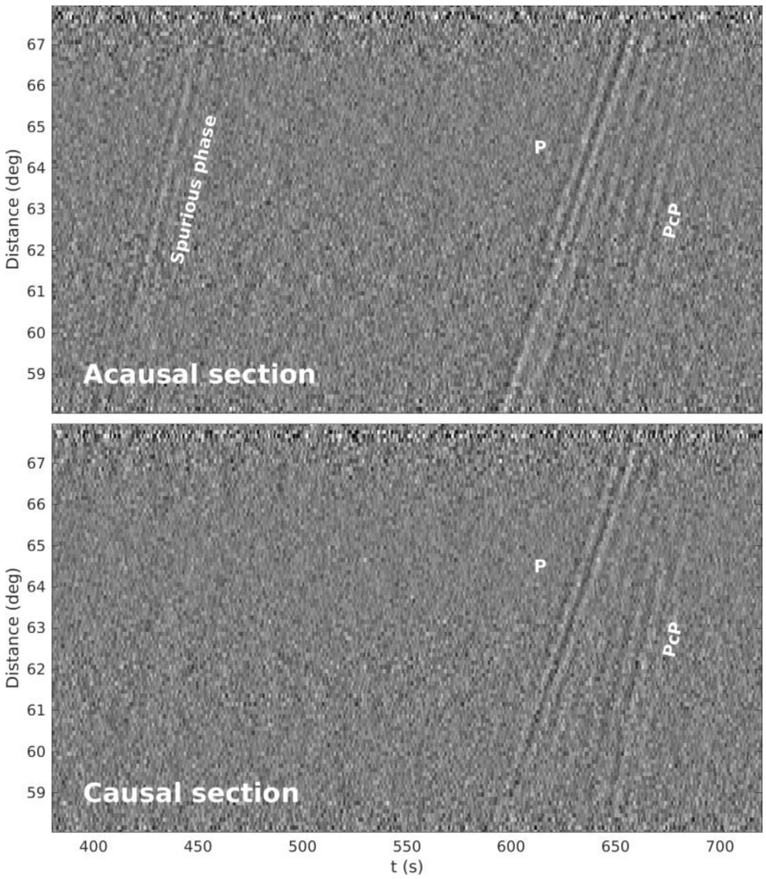

Figure S4. Broadband sections of the acausal and causal parts of the vertical-vertical noise correlations stacked in 0.1° distance bins. The acausal section for negative time lags is flipped to share a common time axis with the causal section. The acausal (causal) correlations correspond to seismic waves travelling from FNET to LAPNET (from LAPNET to FNET).

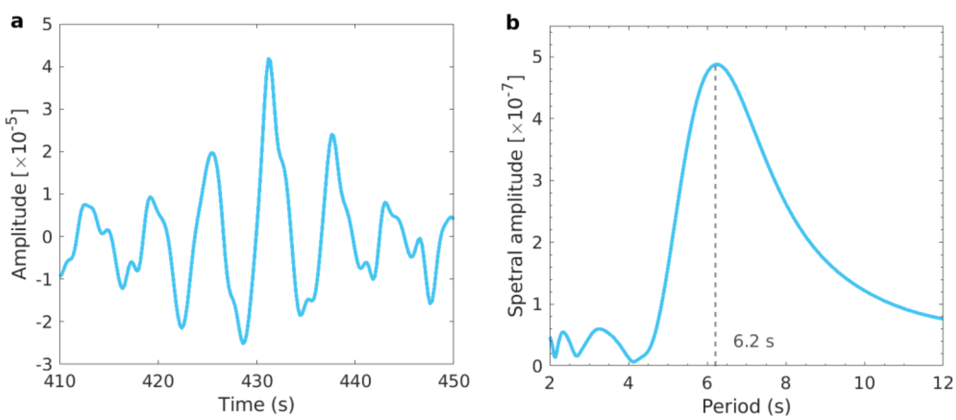

Figure S5. (a) Double-beamed waveform and (b) amplitude spectrum of the spurious phase in the broadband (1-100 s).

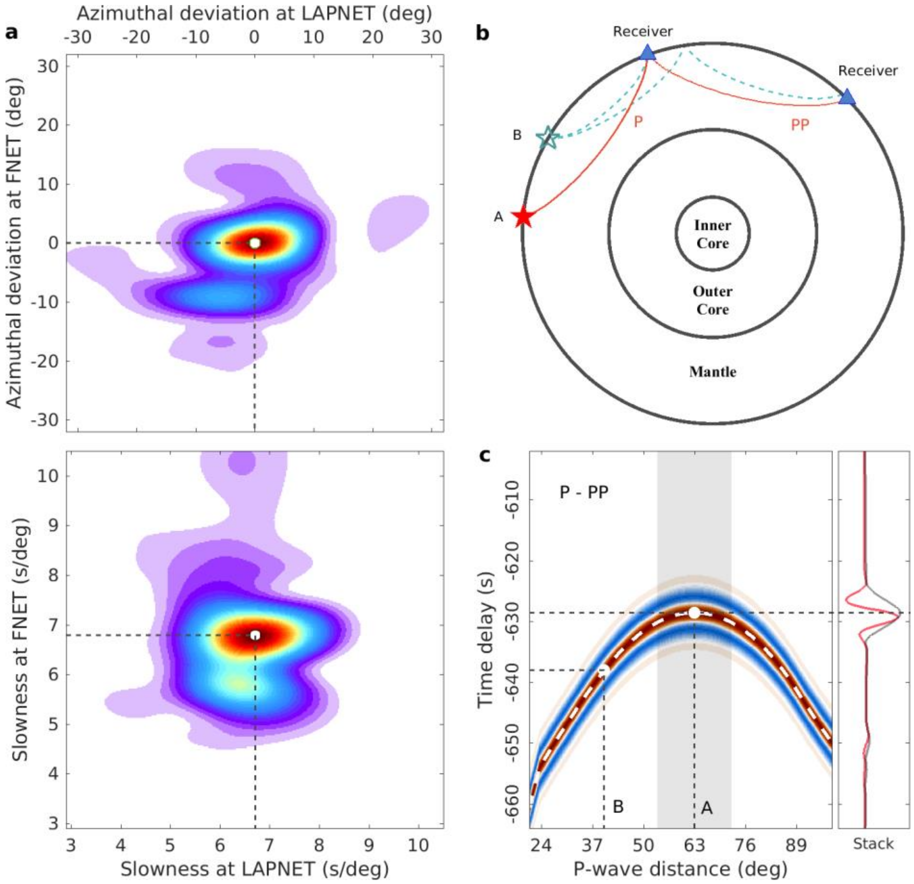

Figure S6. (a) Results of double-array slowness analysis for the acausal P wave. The optimal estimates are marked by white dots. (b) Ray paths of the correlated P and PP waves from distributed sources. Triangles are two receivers 63° apart. Stars represent noise sources. Source *A* is placed at the stationary location. The P wave to the first receiver and the PP wave to the second receiver have a common slowness and a common P path. The correlation operator cancels the common path and extracts the phase delay between two receivers. Label *B* denotes any noise source on the global surface outside the stationary-phase region. Correlations between higher-order multiples like PP-PPP can also give rise to P wave but are neglected for simplicity. (c) Reconstruction of the inter-receiver P wave from the correlations between P and PP waves by source averaging, explained by the tranditional stationary-phase theory. Dashed white line indicates the theoretical P-PP time delays for distributed noise sources, calculated using *Taup* and *IASP91*. The stationary location corresponds to the extreme point on the time-delay curve. Columns of the background image are synthetic P-PP correlations for distributed sources. Red and blue colors signify positive and negative amplitudes, respectively. The source-wise correlation functions are synthesized by convolving the time delays with a 6.2 s period Gaussian-modulated sinusoidal pulse. Amplitude variations with distance are neglected. Shaded area delineates the stationary-phase region that contribute to the reconstruction of the inter-receiver P wave. Amplitudes in P-PP correlations for sources outside the stationary-phase region cancel out by the averaging. The inter-receiver P-wave signal (red) and its envelope (black) are plotted in the right panel. The time at the maximum of the envelope matches exactly with the theoretical travel time of the P wave.

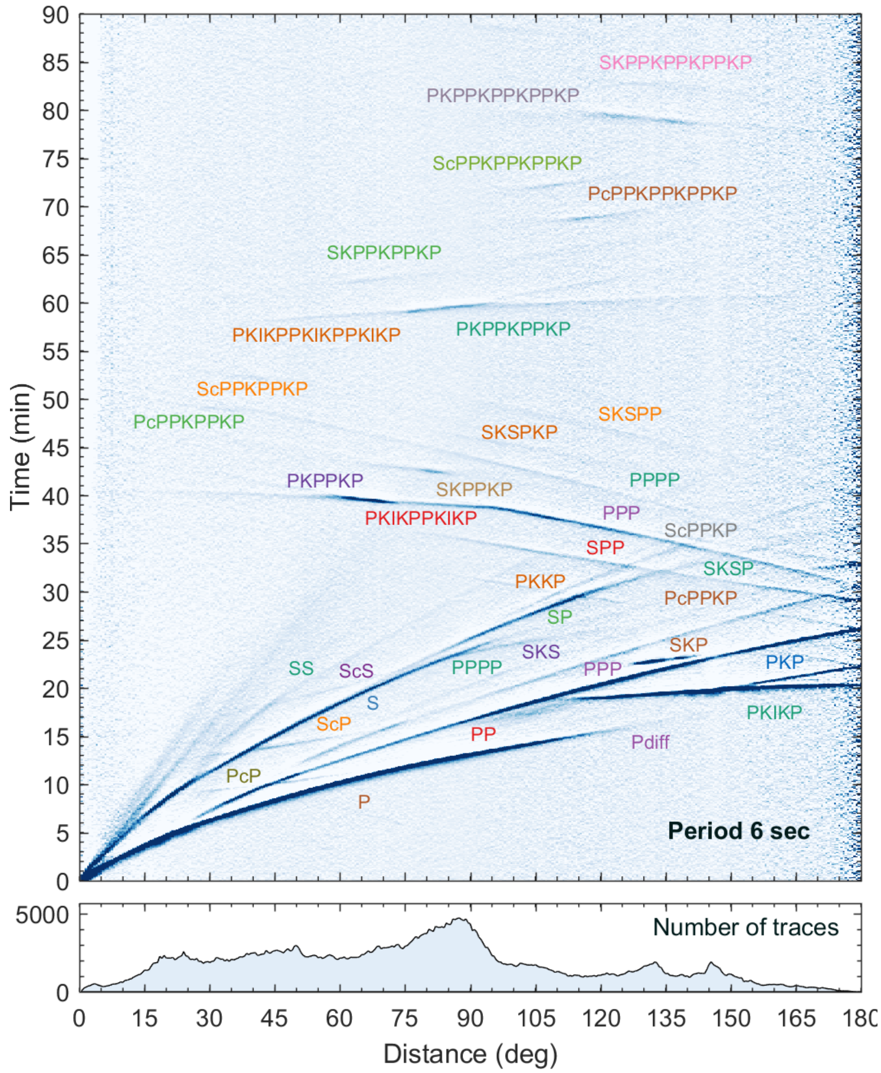

Figure S7. Global stacks of vertical components of seismograms selected from records of more than 2,500 shallow earthquakes (event depth shallower than 50 km and magnitude no less than 5.4) occurring between 1995 and 2013. The seismograms are filtered around 6 s period and converted into traces of STA/LTA ratios. The STA/LTA traces are binned by epicentral distances in an interval of 0.5° and normalized for plotting. More details concerning the data processing and data retrieval can be found on the IRIS Data Services Products website. Discernible seismic body phases are labeled on the image.

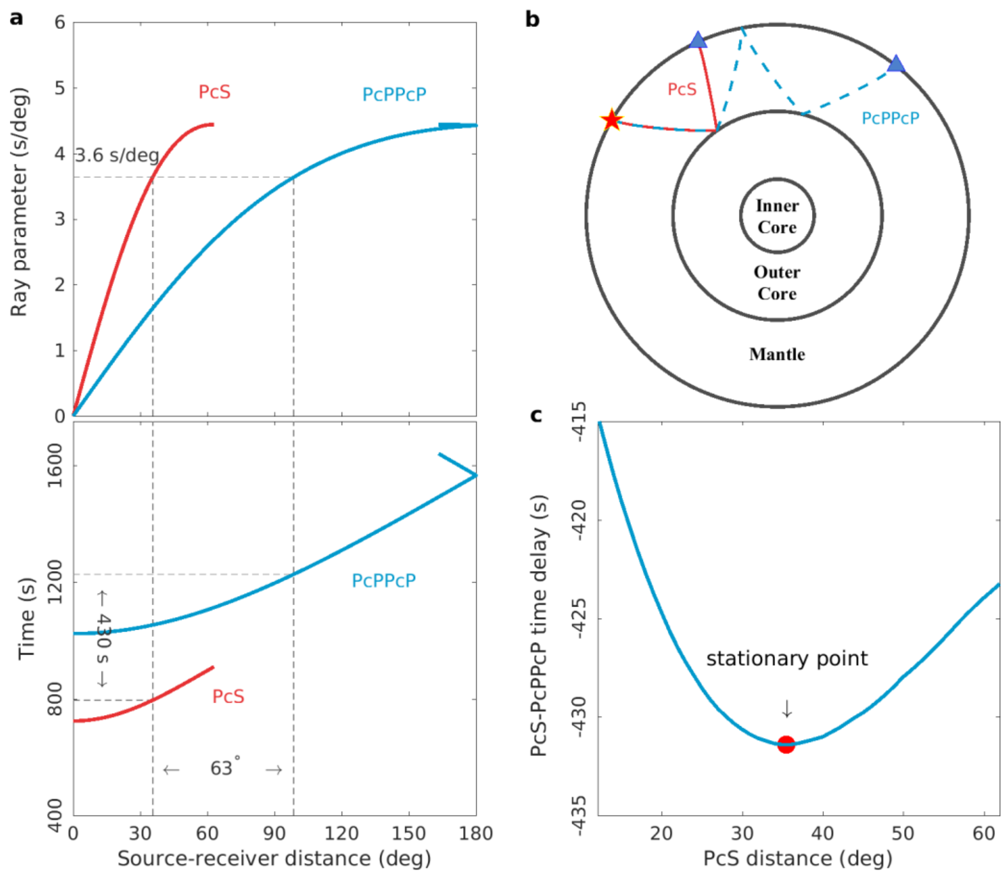

Figure S8. (a) Theoretical curves of ray parameters and travel times of PcS and PcPPcP. (b) Ray paths of PcS and PcPPcP from source at stationary location. (c) PcS-PcPPcP time delays for distributed sources. The PcS-PcPPcP correlation can produce a signal at 430 s time delay and 63° inter-station distance, but the slownesses are quite different from out slowness estimates in Figure 2a. In the global section of coda correlations [see Figure 2 of Phạm et al. (2018)], there is a spurious arrival at ~430 s time delay and 63° distance. Phạm et al. (2018) ascribed the arrival to cS-cPPcP (or s-pPcP in IASPEI convention) correlations for sources distributed on the core-mantle boundary. The PcS-PcPPcP correlation here is an equivalence to their cS-cPPcP correlation, but for sources on the surface. PcS and PcPPcP waves could be prominent in the period band of 30-50 s in the coda waves of large earthquakes, but are faint phases in the ambient wavefield. Therefore, it is logical that we do not observe the PcS-PcPPcP correlations from the ambient noise correlations.